Development of a Precipitation Climate Record from Spaceborne Precipitation Radar Data. Part II: Temporal Adjustment of the Calibration Change Using the Ocean Normalized Radar Cross Section

KAYA KANEMARU,[a] TOSHIO IGUCHI,[b] TAKESHI MASAKI,[c] NAOFUMI YOSHIDA,[c] AND TAKUJI KUBOTA[d]

[a] *Radio Research Institute, National Institute of Information and Communications Technology, Koganei, Japan*
[b] *Graduate School of Engineering, Osaka University, Suita, Japan*
[c] *Remote Sensing Technology Center of Japan, Tsukuba, Japan*
[d] *Earth Observation Research Center, Japan Aerospace Exploration Agency, Tsukuba, Japan*

(Manuscript received 9 November 2023, in final form 11 July 2024, accepted 12 August 2024)

ABSTRACT: We analyze the calibration stability of the 17-yr precipitation radar (PR) data on board the Tropical Rainfall Measuring Mission (TRMM) satellite to develop a precipitation climate record from the spaceborne precipitation radar data of the TRMM and following satellite missions. Since the PR measures the normalized radar cross section (NRCS) over the ocean surface, the temporal change in the NRCS whose variability is insensitive to the sea surface wind is regarded as the temporal change of the PR calibration. The temporal change of the PR calibration in TRMM, version 7, is found to be 0.19 dB decade^{-1} from 1998 to 2013. The calibration change is simply adjusted to evaluate the NRCS time series and the near-surface precipitation trend analysis within the latitudinal band between 35°S and 35°N. The NRCS time series at nadir and off-nadir are uncorrelated before the calibration adjustment, but they are correlated after the adjustment. The 0.19 dB decade^{-1} change of the PR calibration causes an overestimation of 0.08 mm day^{-1} decade^{-1} or 2.9% decade^{-1} for the linear trend of the near-surface precipitation. Even after the adjustment, agreement of the results among the satellite products depends on the analysis period. The temporal stability of the data quality is also important to evaluate the plausible trend analysis. The reprocessing of the PR data in TRMM, version 8 (or later), takes into account the temporal adjustment of the calibration change based upon the results of this study, which can provide more credible data for a long-term precipitation analysis.

SIGNIFICANCE STATEMENT: The stability of long-term data is very important for climate research so that an account of temporal calibration changes in the sensor must be made. In this study, we investigate the calibration stability of the TRMM PR data and evaluate its impact on the precipitation trend analysis. The temporal change of the PR calibration is estimated to be 0.19 dB decade^{-1}. Compensating for this change improves the consistency of precipitation trend analysis between the PR and other precipitation datasets. The reprocessed PR data provide more probable data for long-term precipitation analysis.

KEYWORDS: Precipitation; Radars/Radar observations; Satellite observations

1. Introduction

Satellite observations have advantages in the global measurement of precipitation and its monitoring. Global precipitation records have been archived for more than 30 years (Xie and Arkin 1997; Ashouri et al. 2015; Adler et al. 2018), thanks to much effort in developing consistent long-term records with different sensors (e.g., Colton and Poe 1999; Wentz et al. 2001; Yan and Weng 2008; Sapiano et al. 2013; Wentz 2013; Berg et al. 2016). In that respect, the instruments on board the Tropical Rainfall Measuring Mission (TRMM) satellite are utilized as a reference to intercalibrate other sensors. The TRMM satellite carried the precipitation radar (PR) and the TRMM microwave imager (TMI) to realize the quantitative measurement of tropical rainfall (Kummerow et al. 1998; Kozu et al. 2001) and operated for 17 years from December 1997 to April 2015 (Takahashi et al. 2016). The long-term operation provided continuous and stable sensor records of the PR and TMI; therefore, ground-based radars are calibrated with the PR (Anagnostou et al. 2001; Kim et al. 2014; Warren et al. 2018; Crisologo et al. 2018; Zhang et al. 2018; Han et al. 2018), and other microwave radiometers are intercompared with the TMI (Wentz 2015; Berg 2017).

The 17-yr record of the PR has potential use for investigating the long-term variability of precipitation characteristics. The PR observes the three-dimensional structure of precipitation over ocean and land surfaces. Although the 17-yr record of the PR is not long enough to discuss long-term changes in precipitation due to global warming, the record can be used to derive the interannual variability of precipitation characteristics such as the vertical structure of precipitation (Schumacher and Houze 2003; Henderson et al. 2017, 2018). The Global Precipitation Measurement (GPM) *Core Observatory* (Hou et al. 2014; Skofronick-Jackson et al. 2017), launched in February 2014, carries the dual-frequency precipitation radar (DPR) as the successor to the TRMM PR (Kojima et al. 2012; Iguchi

Denotes content that is immediately available upon publication as open access.

Corresponding author: Kaya Kanemaru, kanemaru@nict.go.jp

DOI: 10.1175/JTECH-D-23-0151.1

2020; Nakamura 2021; Masaki et al. 2022). The DPR consists of Ku-band (13.6 GHz) and Ka-band (35.5 GHz) PRs (KuPR and KaPR, respectively). Since the operating frequency of the PR is also Ku band (13.8 GHz), the PR and KuPR can provide a precipitation data record observed by the Ku-band spaceborne precipitation radars longer than 26 years. The precipitation record by combining the PR and KuPR data was analyzed to investigate the decadal variability of precipitation (Takahashi and Fujinami 2021; Ji et al. 2022).

The sensitivity of the TRMM PR changed slightly over the 17-yr period. For example, the PR data have significant discontinuities associated with the increase in TRMM satellite altitude (TRMM orbit boost) in August 2001 (Takahashi and Iguchi 2004; Shimizu et al. 2009) and with the switching to redundant electronics in June 2009 (TRMM PR Team 2011). In addition, the fuel for the orbit maintenance was finally exhausted in July 2014; since then, the satellite gradually descended and reentered the atmosphere in June 2015 (Takahashi et al. 2016).

To develop a homogeneous data record using the PR and KuPR, Kanemaru et al. (2017) mitigated the discontinuity of the PR data encountered in May 2009. In this paper, we focus on the calibration stability of the PR. Although the calibration accuracy obtained for the PR is within ±1 dB (Kozu et al. 2001) and its stability over time (Takahashi et al. 2003; Komukai et al. 2010) is better than those of ground-based radars (Warren et al. 2018), the robust calibration stability of the PR over the entire TRMM period is necessary to evaluate the long-term variability of precipitation. A requirement of the calibration stability for climate analysis is simply estimated below. The power law between the radar reflectivity factor Z (in mm^6 m^{-3}) and the precipitation rate R (in mm h^{-1}) is given by $Z = aR^b$, where the coefficients of a and b depend on the drop size distribution of precipitation events. Since the radar virtually measures Z, a calibration error in Z causes a bias in R. From the Z–R relation, the relative bias of R (ΔR) due to the calibration error in Z is obtained as

$$\Delta R = 10^{0.1\delta/b} - 1,$$

where δ is the calibration error (in dB) of the estimated Z in dBZ. Figure 1 shows ΔR when $b = 1.3$ and 1.6. The range of b covers a variation of Z–R relations depending on the precipitation type (Kozu et al. 2009). The calibration error propagates $|\Delta R|$ by about 13%–20% dB^{-1}. On the other hand, an observational trend of the global mean surface temperature from 1980 to 2020 is given as 0.76-K change or ~0.2 K decade^{-1} (IPCC 2021). The projected change in global mean precipitation with global surface air temperature is estimated as 2.1%–3.1% K^{-1} in general circulation models (IPCC 2021). The expected precipitation change due to global warming may be inferred as 2% K^{-1} × 0.2 K decade^{-1} or 0.4% decade^{-1}. Therefore, the calibration stability of the radar required to detect the precipitation change due to global warming is

$$\left|\frac{d\delta}{dt}\right| = \left|\frac{dR}{dt}\right|\left|\frac{d\delta}{dR}\right| \approx \frac{0.4(\%\ \text{decade}^{-1})}{20(\%\ \text{dB}^{-1})} = 0.02(\text{dB decade}^{-1}).$$

The calibration stability of the PR was monitored with the normalized radar cross section (NRCS) or σ^0 over the oceans (Takahashi et al. 2003; Komukai et al. 2010), but this task was conducted to confirm that the radar satisfied the mission requirement that the measurement accuracy was within ±1 dB. More strict calibration stability is required to utilize data of the spaceborne precipitation radars for a long-term precipitation analysis.

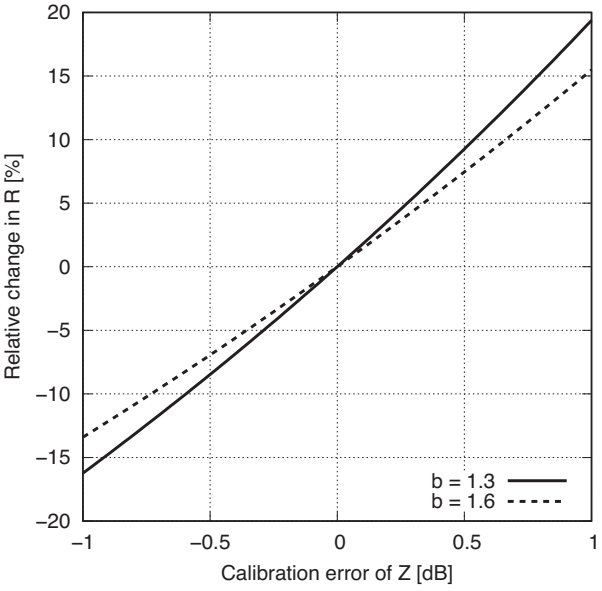

FIG. 1. Relative bias of R (%) due to the calibration error in Z (dB) obtained from Z–R relations. The solid and dashed lines are for $b = 1.3$ and $b = 1.6$, respectively.

The adjustment of the temporal change in the calibration is required to utilize the precipitation radar record for climate analysis. In this study, we aim to seek the temporal change in the PR calibration with the σ^0 statistics over the oceans and evaluate the impact of its adjustment on the temporal change in precipitation estimates. The data and method used are introduced in section 2. The results are presented in section 3. The impacts of the temporal adjustment of the calibration change on the precipitation variability are discussed by using other rainfall products in section 4. A summary of the results is presented in section 5.

2. Data and method

a. Data used

The PR 2A21 (JAXA 1997b) and 2A25 (JAXA 1997a) products of TRMM, version 7, released in 2011 are used in the current study. TRMM, version 7, was the final version in the TRMM era. TRMM, versions 8 and 9, released in 2018 and 2022, respectively, was based upon the GPM algorithm developments in the GPM era. In this paper, version 7 was used to take advantage of the accumulation made during the TRMM era. However, the results obtained here can be used in subsequent versions in the GPM era and have been utilized as described later. The 2A21 products contain the measured σ^0 (σ^0_m) computed using the surface scattering radar equation

(Kozu 1995; Meneghini et al. 2000) and the precipitation flag. The PR 2A25 products contain precipitation rates as hybrid estimates by the Hitschfeld–Bordan method and the surface reference technique (Iguchi et al. 2000, 2009); then, the precipitation rates for stratiform and convective types classified using the 2A23 algorithm (Awaka et al. 2009) are estimated from different assumptions of drop size distribution obtained by Kozu et al. (2009). The precipitation rate at the near surface (nearSurfRain), that is, defined as the lowest level in the clutter free ranges, is analyzed in the current study.

The state of the ocean surface is required to estimate the temporal change in the PR calibration from the σ^0 statistics. In this study, we use the instantaneous 0.25° × 0.25° gridded TMI estimates of sea surface wind (SSW), sea surface temperature (SST), column water vapor (CWV), and cloud liquid water path (CLWP) obtained from the Remote Sensing System (RSS), version 7.1, product (Wentz 2015; Wentz et al. 2015) and the Goddard profiling (GPROF) 2010 version 2 product (Kummerow et al. 2011). The current analysis utilizes the SSW data from different providers to evaluate validity of the current method. Since the RSS products contain two SSW estimates with or without the 10.7-GHz channel, the current study analyzed the SSW estimates without the 10.7 GHz whose spatial resolution is finer than that with the 10 GHz.

The TMI 2A12 precipitation products in TRMM, version 7 (Kummerow et al. 2001; TRMM 2011), and Global Precipitation Climatology Project (GPCP), V3.2 (Huffman et al. 2020, 2023), are compared with the PR precipitation products for the linear trend analysis. For the linear trend analysis of precipitation, the instantaneous precipitation data of 2A12/2A25 are averaged monthly on 2.5° × 2.5° grid to normalize the difference in sampling numbers at different locations. After that, area averages within the latitudinal band between 35°S and 35°N are computed from the 2.5° × 2.5° gridded data.

b. Calibration

The PR had been calibrated and monitored by a calibrator several times a year (Takahashi et al. 2003; Masaki et al. 2022) to satisfy the mission requirement of measurement accuracy of Z within ±1 dB. Takahashi et al. (2003) showed that the calibration stability of the PR with the calibrator was confirmed to be within ±0.5 dB. Thus, the temporal change of the PR calibration can be extracted by the calibrator only when the magnitude of the calibration change is much larger than 0.5 dB. Moreover, since the PR calibration with the calibrator was conducted only a few times a year, the short-term changes in the PR calibration are difficult to detect. For those reasons, small changes in the PR calibration over time are not compensated for in TRMM, version 7, except for the difference in the receiver system of the PR, which was switched in June 2009 (TRMM PR Team 2011).

In this study, we estimate the temporal change in the PR calibration by using measured σ^0 over the oceans as a reference (e.g., Silberstein et al. 2008). The PR scans from 17.04° to −17.04° from nadir with 49 angle bins at the interval of 0.71° in the cross-track direction and measures σ^0 from incidence angles from 0° to 18° consisting of 25 angles. The measured σ^0 (i.e., σ^0_m) at the incident angle θ_z is calculated by the modified equation of Kozu (1995):

$$\sigma^0_m(\theta_z) = \frac{2^9 \ln(2)\pi^2 L \cos(\theta_z) r_s^2}{\lambda^2 G_r G_t \theta_{bp} \phi_b} \frac{P_{r,s}(r_s)}{P_t} = C_s \frac{P_{r,s}(r_s)}{P_t}, \quad (1)$$

where λ is the wavelength, L is the band path filter loss, G_r is the receiving antenna gain, G_t is the transmitting antenna gain, ϕ_b is the −6-dB width of the two-way antenna pattern in the along-track direction, r_s is the range from the radar to the Earth's surface along the center of the radar beam, P_t is the peak transmitting power, and $P_{r,s}(r_s)$ is the received signal power at the range of r_s, which is given as $P_r - P_n$ where P_r is the received power and P_n is the noise power, respectively. The effective cross-track beamwidth θ_{bp} is expressed as follows:

$$\frac{1}{\theta_{bp}^2} = \frac{1}{\theta_b^2} + \frac{1}{\theta_p^2}, \text{ and } \theta_p = \frac{c\tau_r}{2} \frac{1}{r_s \tan\theta_z},$$

where θ_b is the −6-dB width of the two-way antenna pattern in the cross-track direction, c is the speed of light in vacuum, and τ_r is the −6-dB width of the received pulse, respectively. Ignored/unknown temporal changes in parameters used in (1) cause the calibration change δ_t. We assume $P_{r,s} \gg P_n$ and then (1) can be written in a simple from as

$$\sigma^0_m(\text{dB}) = C_s(\text{dB}) + P_r(\text{dBm}) - P_t(\text{dBm}) + \delta_t(\text{dB}). \quad (2)$$

Although we cannot know temporal changes in each term in (2), this study estimates the temporal change of the net calibration error.

On the other hand, the measured Z (i.e., Z_m) is expressed as follows (Iguchi et al. 2023):

$$Z_m = \frac{2^{10} 10^{18} \ln(2)\lambda^2 r^2}{\pi^3 c G_t G_r \theta_b \phi_b \tau_t |K|^2} \frac{P_{r,s}(r)}{P_t} = C_p \frac{P_{r,s}(r)}{P_t}, \quad (3)$$

where r is the range distance, τ_t is the transmitted pulsewidth, and $|K|^2$ is the dielectric factor, respectively. If we assume $P_{r,s} \gg P_n$ and introduce δ_t, (3) can be written in decibel as

$$Z_m(\text{dBZ}) = C_p(\text{dBZ}) + P_r(\text{dBm}) - P_t(\text{dBm}) + \delta_t(\text{dB}). \quad (4)$$

The current study assumes that δ_t equally affects the surface and precipitation echoes and that δ_t originates in the unconsidered changes in the radar parameters and the received and transmitted powers.

c. Analysis method

The temporal change in σ^0 statistics over the oceans obtained from the PR data is caused not only by the calibration change but also by the changes in the ocean surface conditions. To distinguish those changes, we consider the characteristics of the quasi-specular theory (Barrick 1974; Valenzuela 1978) at a small incidence. The σ^0 may be expressed in this theory as

$$\sigma^0(\theta_z) = \frac{|\Gamma|^2}{s\cos^4\theta_z}\exp\left(-\frac{\tan^2\theta_z}{s}\right), \quad (5)$$

where Γ is the Fresnel reflection coefficient at the nadir incidence and s is the mean square slope which is closely related to the SSW. Differentiating the natural logarithm of σ^0 with respect to s in (5), we have

$$\frac{\partial \ln\sigma^0}{\partial s} = \frac{1}{s^2}(\tan^2\theta_z - s), \quad (6)$$

where $\partial\ln\Gamma/\partial s$ is assumed to be zero because Γ depends on only SST and sea surface salinity (SSS) as a function of λ (Klein and Swift 1977). Inserting $s = \tan^2\theta_z$ in (6) yields

$$\left.\frac{\partial \ln\sigma^0}{\partial s}\right|_{s=\tan\theta_z} = 0. \quad (7)$$

The σ^0 variability becomes insensitive to the SSW within the limits of its specific ranges at $\theta_z \simeq 10°$ (Wentz et al. 1984; Li et al. 2002; Freilich and Vanhoff 2003). Since σ^0 should be invariant in specific SSW conditions, the temporal change in PR σ^0 in these conditions can be characterized as the temporal change in the PR calibration. To confirm the σ^0 variability, the geophysical model function (GMF) of σ^0 as a function of the incident angle θ_z and the SSW (i.e., U_{10}) is generated as

$$\sigma^0 \simeq \mathrm{GMF}(\theta_z, U_{10})_{\mathrm{pol}},$$

where the subscript "pol" is the polarization of the radar. The polarization of both PR transmitted and received waves is horizontal.

An attenuation for the atmospheric gas (water vapor and oxygen) and the hydrometeor (cloud and precipitation) also causes the apparent σ^0 variability. The GMF statistics is constructed by taking into account the attenuation. Attenuation due to oxygen molecules is ignored in this study because it is very small (<0.1 dB) and almost constant (Iguchi et al. 2009). Attenuation due to water vapor is not negligibly small in the Ku band so that the two-way attenuation due to water vapor is simply corrected by using the formula in Iguchi et al. (2009) as

$$\sigma^0(\mathrm{dB}) = \sigma_m^0(\mathrm{dB}) + 4.94\times10^{-3}\times\mathrm{CWV(mm)}.$$

Data that include precipitation echoes are excluded for the generation of the GMF by using the precipitation flag in the 2A21 products. The precipitation flag is set when precipitation echoes exist along the vertical profile (Kumagai et al. 1996). Data that may be affected by the attenuation caused by cloud liquid water, light precipitation (<0.7 mm h^{-1}) whose signal cannot be detected by the PR, and precipitation signals masked by ground clutter of the PR at low altitude (1–2 km) are excluded when the TMI's CLWP is higher than 0.5 mm.

The TRMM satellite carries the PR and TMI so that the PR σ^0 in nonprecipitating pixels and the SSW, SST, CWV, and CLWP estimates of the TMI are collocated simultaneously. The σ^0 and θ_z data with the original footprint size of 4–5 km are averaged together into an instantaneous 0.25° × 0.25° resolution. The gridded PR data are analyzed to match with the gridded TMI data.

3. Results

Figure 2 shows the statistics of the GMF as a function of θ_z and U_{10} obtained from gridded instantaneous data of PR and TMI. Note that the TMI products provided by RSS are analyzed in Fig. 2. Figure 2 is generated from the data from 2002 to 2008 (7 years) because the quality of the PR data is the same during the period between the TRMM orbit boost in August 2001 and the switching to redundant electronics of the PR in June 2009. The statistics of the GMF is generated for each 0.75° bin of θ_z from 0.0° to 18.0° (the incidence angle increment of the PR is approximately 0.75°) and for each 0.2 m s^{-1} of U_{10} from 0 to 15 m s^{-1}. The average σ^0 shown in Fig. 2a is similar to those obtained in previous studies (e.g., Li et al. 2002; Freilich and Vanhoff 2003; Komukai et al. 2010; Munchak et al. 2016). In Fig. 2b, small standard deviations are found at around moderate SSWs from 5 to 10 m s^{-1} and moderate incident angles from 6° to 12°. The fading noise of σ_m^0 in each measurement is given as $5.57/\sqrt{64} \simeq 0.7$ dB, where 64 is the independent sampling number for the PR. The current analysis utilizes the 0.25° × 0.25° average so that the fading noise is lower than 0.4 dB. In calm winds lower than 5 m s^{-1}, σ^0 rapidly decreases with an increase in θ_z, and its standard deviation increases drastically because the σ^0 variability is affected by swell rather than waves induced by local wind. Much of the collocation in Fig. 2c is distributed around 5–9 m s^{-1}. The sensitivities of σ^0 with respect to θ_z (Fig. 2d) and to U_{10} (Fig. 2e) are confirmed to identify insensitive domains against θ_z and U_{10}. Except for calm winds with speeds less than 5 m s^{-1}, $\partial\sigma^0/\partial\theta_z$ monotonically changes from 0 dB per degree at $\theta_z = 0°$ to −1 dB per degree at $\theta_z \sim 10°$. A stepwise change in $\partial\sigma^0/\partial\theta_z$ from 10° to 11° of θ_z is caused by the existence of twice range-oversampled data (Kanemaru et al. 2020). For θ_z from 7.5° to 12°, insensitive domains of $\partial\sigma^0/\partial U_{10}$ are distributed around moderate SSWs from 4 to 12 m s^{-1} depending on θ_z because the insensitive domain is a function of both θ_z and s as shown in (7).

By taking into account the roll angle error of the TRMM satellite (Wentz 2015; Stocker et al. 2018), the stepwise change in $\partial\sigma^0/\partial\theta_z$, and the large number of collocations, we use σ^0 statistics at $\theta_z = 9.0° \pm 0.375°$ and $U_{10} = 8.0 \pm 0.1$ m s^{-1} to estimate the temporal change in the PR calibration. In this domain, the sensitivities with respect to θ_z and U_{10} are $\partial\sigma^0/\partial\theta_z = -0.832$ dB per degree and $\partial\sigma^0/\partial U_{10} = -0.079$ dB $(\mathrm{m\ s^{-1}})^{-1}$, respectively. Although $\partial\sigma^0/\partial\theta_z$ is somewhat large, in this study, we average σ^0 obtained from the cross-track scan of positive and negative angles to cancel out any possible roll error. On the other hand, the standard deviation of the TMI SSW compared with ocean buoy measurements is 0.77 m s^{-1} (Wentz 2015) so that the error of the TMI SSW causes the error of σ^0 as $|0.079|$ dB $(\mathrm{m\ s^{-1}})^{-1} \times (0.77\ \mathrm{m\ s^{-1}}) = 0.061$ dB, which is smaller than the standard deviation of the average σ^0. Note that the standard deviation of the TMI CWV compared with the global positioning system (GPS) measurements is 2.07 mm (Wentz 2015) so that the error in the attenuation estimates due to the uncertainty in CWV

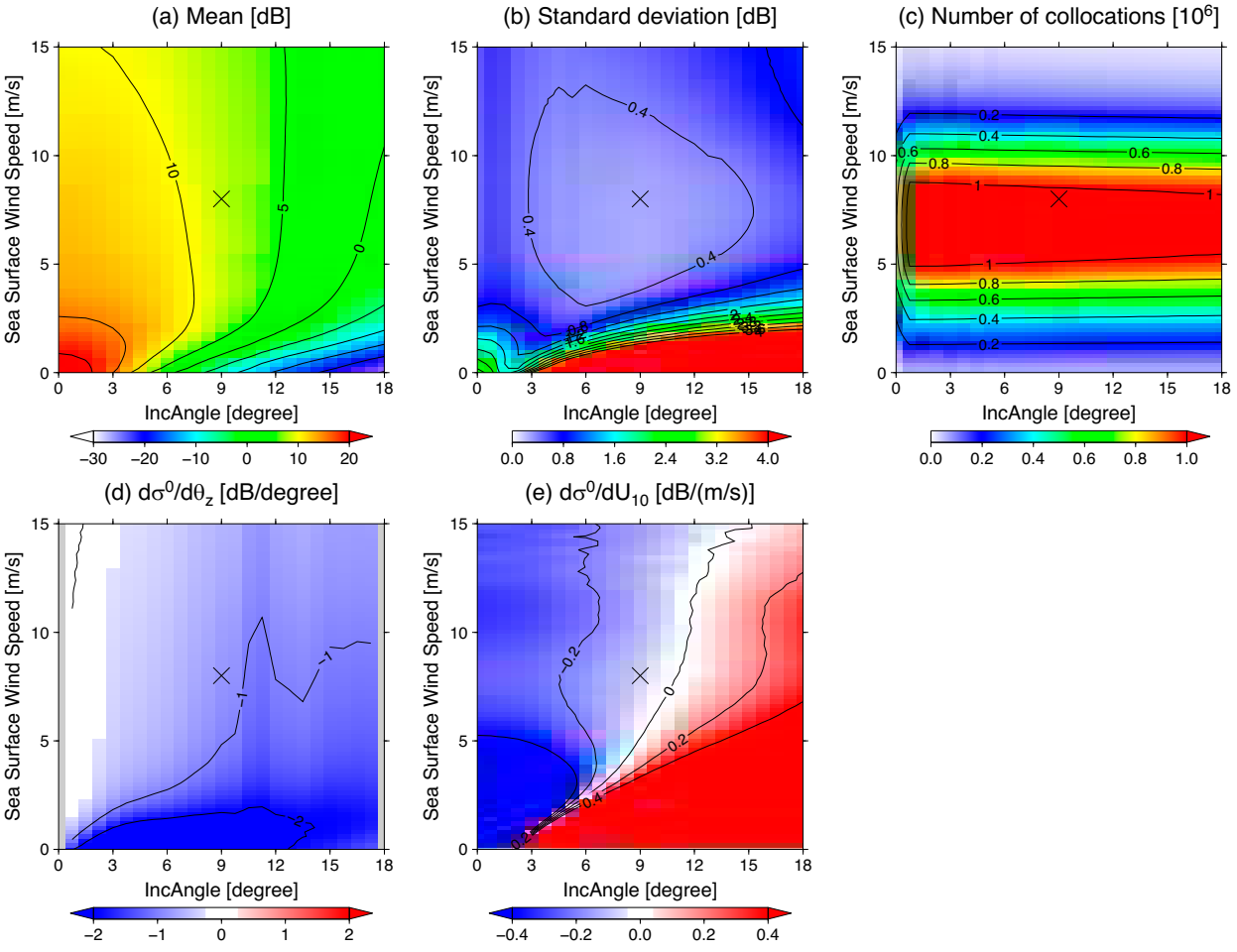

FIG. 2. GMF matched with PR and TMI. The horizontal axis is θ_z obtained by the PR. The vertical axis is U_{10} obtained by the TMI. The σ^0 statistics is the 7-yr average from 2002 to 2008. Bin sizes are 0.75° for θ_z and 0.2 m s^{-1} for U_{10}. Cross symbol is located at $U_{10} = 8$ m s^{-1} and $\theta_z = 9.0°$. (a) Mean of σ^0 (dB). (b) Standard deviation of σ^0 (dB). (c) Collocated number (10^6). (d) Sensitivity of σ^0 to θ_z or $\partial\sigma^0/\partial\theta_z$ (dB per degree). (e) Sensitivity of σ^0 to SSW or $\partial\sigma^0/\partial U_{10}$ [dB (m s^{-1})$^{-1}$]. Gray color indicates missing values.

is given as $4.94 \times 10^{-3} \times 2.07 = 0.01$ dB. Therefore, the error of CWV is virtually ignored for the σ^0 variability.

Figure 3 shows the time series of the σ^0 statistics at $\theta_z = 9.0° \pm 0.375°$ and $U_{10} = 8.0 \pm 0.1$ m s^{-1}. To evaluate the algorithm dependence of the SSW estimates, three types of TMI-SSW data, which are the estimates of the RSS data obtained from the 18.7-GHz channel (black line) and GPROF data (blue line), are compared. Since σ^0 sampled at $U_{10} = 8.0$ m s^{-1} of the GPROF data is 0.1 dB higher than that of the RSS data, the σ^0 statistics obtained from the GPROF data is offset by −0.1 dB. The time series of the σ^0 statistics obtained from the two types of datasets agree well except for small fluctuations. We can clearly find four abrupt changes and a trend of the temporal change in the PR calibration over the TRMM period. The first abrupt change in February 1998 corresponds to the time when the internal attenuator was switched from 6 to 9 dB (Takahashi and Iguchi 2008). The third abrupt change in June 2009 corresponds to the time of switching from the original A-side electronics to the redundant B-side electronics (Kanemaru et al. 2017). The first and third abrupt changes are caused by errors in the PR calibration because the calibration curves before the events are different from those after the events. The second abrupt change is related to the σ^0 decrease for a given scan angle with a small increase in θ_z caused by the TRMM orbit boost from 350 to 403 km and by the quality degradation of the PR data at 403 km due to the beam-mismatch correction error (Tagawa et al. 2009; Kanemaru et al. 2019). The fourth abrupt change[1] in February 2015, which is based on the comparisons only with the GPROF data because the RSS data were not available after December 2014, is caused for the same reason for the second abrupt change when the satellite altitude changed from 403 to 350 km.

[1] The PR normal observations were temporally stopped from the end of the 403-km operation in October 2014 to the beginning of the 350-km operation in February 2015 (Takahashi et al. 2016). The PR observations at 350 km were made for one and a half months from the middle of February to the end of March 2015.

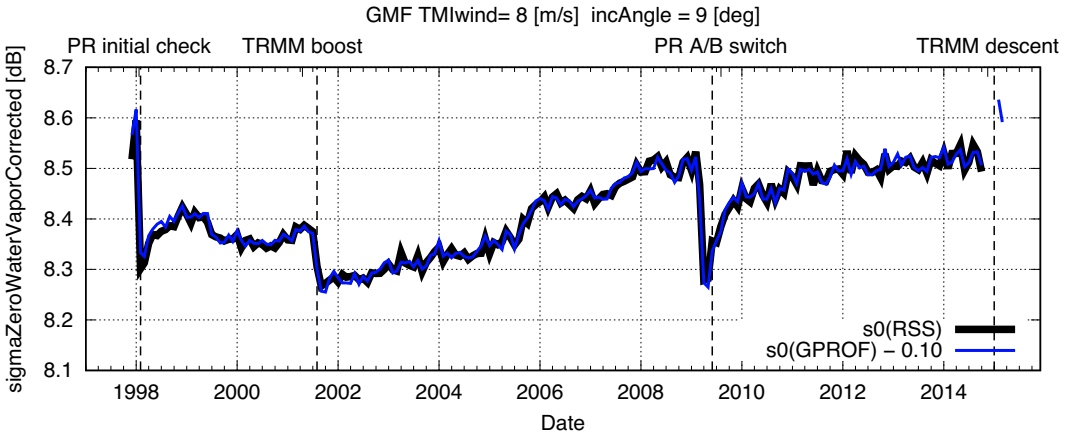

FIG. 3. Time series of the monthly average of σ^0 with water vapor attenuation corrected at $\theta_z = 9.0°$ and $U_{10} = 8\ \mathrm{m\ s^{-1}}$. The colored lines indicate the different SSW estimates of the RSS data obtained (black thick line) and the GPROF data (blue line).

The gradual increases in σ^0 by 0.2 dB from 2002 to 2008 and by 0.1 dB from 2010 to 2014 are found. These changes may be due to the aging of the analog-to-digital converter. Kanemaru et al. (2017) analyzed the time series of the PR noise power from September 2001 to July 2014 and found increases in the noise power by ~0.2 dB from 2002 to 2008 and by ~0.05 dB from 2010 to 2014. The coincident changes between σ^0 and noise power may be inferred as a change in the offset of the calibration curve.

Figure 4 shows the time series of σ^0 anomalies and their dependence on the SST because σ^0 at Ku band slightly changes with Γ as a function of SST. Note that the impacts of SSS on Γ at Ku band are very small and ignored in the current analysis. To mitigate the reduction in the number of collocations, σ^0 is averaged with SSWs for 7–8 m s^{-1} and SSTs for every 2°C and is smoothed using a 3-month average. The σ^0 averages sampled with different SSTs are subtracted from the σ^0 average using the RSS-based SSW data. Since the σ^0 statistics is averaged with SSWs from 7 to 8 m s^{-1}, the offsets are slightly higher than zero. The small SST dependence of σ^0 is found within ~0.05 dB. Therefore, the time series of the σ^0 statistics in Fig. 3 are robustly connected with the temporal change of the PR calibration except for the abrupt changes related to the TRMM orbit boost and descent.

4. Discussion

In this section, we evaluate the impacts of the temporal change of the PR calibration on the time series of the σ^0 and R statistics. To compensate for the temporal change of the PR calibration shown in Fig. 3, the adjustment factor AF is introduced as shown in Fig. 5a and is determined to be an anomaly from the σ^0 statistics in June 2014. Since the abrupt change in

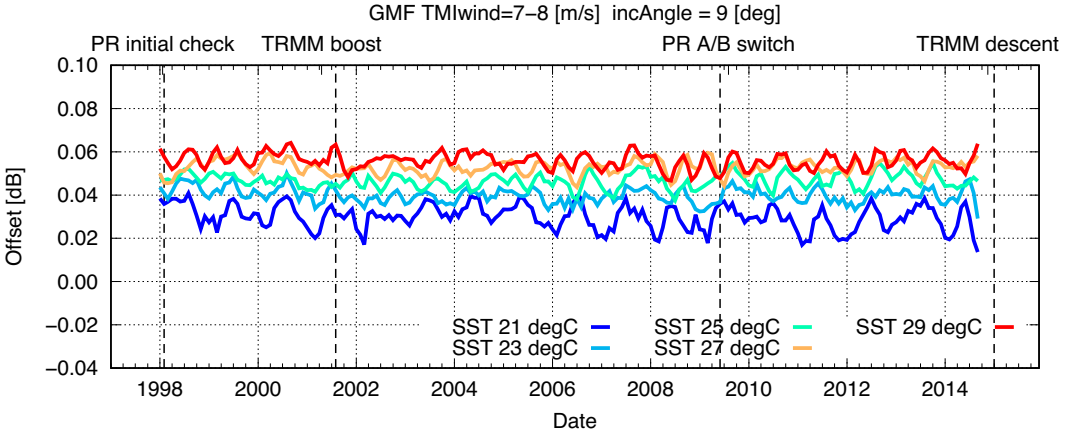

FIG. 4. As in Fig. 3, but for anomalies of σ^0 sampled with SSWs for 7–8 m s^{-1} and SSTs for every 2°C from the result of the black line in Fig. 3. The colors correspond from lower SST (blue) to higher SST (red). The data are smoothed using a 3-month average.

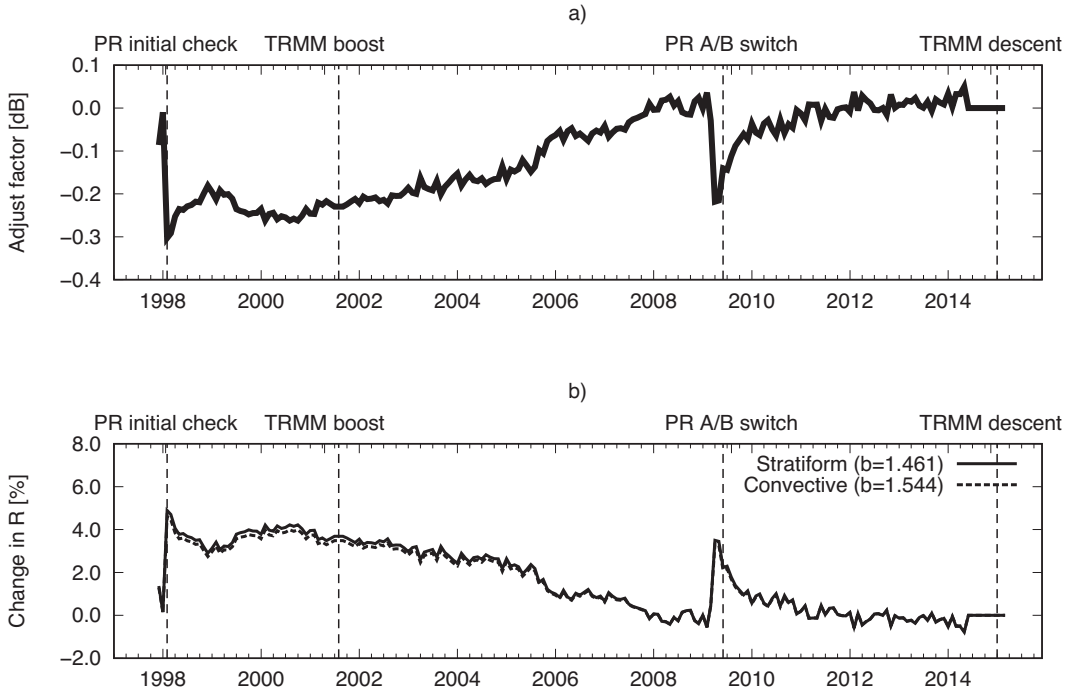

FIG. 5. (a) Time series of adjustment factor (dB). (b) As in (a), but for the factors of ΔR (%) for stratiform (solid line) and convective (dashed line) types.

August 2001 is caused by the change of the satellite altitude from 350 to 403 km, this change is not contained in AF and is removed to match the σ^0 average between July and September in 2001. After June 2014, AF is set to zero.

a. Impacts on σ_m^0

The original data of σ_m^0 (i.e., $\sigma_{m,\mathrm{org}}^0$) are compensated for with AF. The adjusted data of σ_m^0 (i.e., $\sigma_{m,\mathrm{adj}}^0$) are given as

$$\sigma_{m,\mathrm{adj}}^0(\mathrm{dB}) = \sigma_{m,\mathrm{org}}^0(\mathrm{dB}) - \mathrm{AF(dB)}. \tag{8}$$

Figure 6 shows monthly time series of σ^0 at the nadir incidence (angle bin 25) and the maximum scan angle at the scan edge (angle bins 1 and 49) in nonprecipitating pixels. In this study, we focus on a long-term change in σ^0; thus, the results are smoothed by a 13-month average to mitigate the seasonal change in σ^0 caused by the SSW change. The original σ^0 time series at the nadir incidence and at the scan edge tend to increase from 2002 to 2008 (black lines in Figs. 6a,b) even when the dependence of σ^0 on the SSW is opposite between $\theta_z = 0°$ and $\theta_z = 18°$ (Li et al. 2002; Freilich and Vanhoff 2003, also seen in Fig. 2e). The correlation coefficient of the original σ^0 between the nadir incidence and scan edge from 2002 to 2013 is computed to be 0.10. In contrast to the original σ^0 time series, the unnatural σ^0 variabilities from 2002 to 2008 are not seen in the adjusted σ^0 time series (blue lines in Figs. 6a,b). The correlation of adjusted σ^0 between the nadir incidence and scan edge is −0.79, which is consistent with the opposite dependence of σ^0 on the SSW between the near-nadir and off-nadir angles.

b. Impacts on Z_m

The original data of Z_m (i.e., $Z_{m,\mathrm{org}}$) are compensated for with AF. The adjusted data of Z_m (i.e., $Z_{m,\mathrm{adj}}$) are given as

$$Z_{m,\mathrm{adj}}(\mathrm{dB}Z) = Z_{m,\mathrm{org}}(\mathrm{dB}Z) - \mathrm{AF(dB)}. \tag{9}$$

As described in section 2b, the temporal change in the PR calibration is assumed as the change in the radar parameters, received power, and transmitting power. Therefore, the adjustment of Z_m gives the fixed value for altitude.

c. Impacts on R at the near surface

The impacts of the adjustment on R are more complicated than those on σ_m^0 and Z_m because R is not calculated from Z_m by using a simple power-law relationship. The conversion from Z_m to R involves the attenuation correction that depends on the entire profile of Z_m and also on the precipitation type. The reprocessing of the precipitation estimates with the adjusted data of Z_m given as (9) is desirable ideally but takes impractically long time. Therefore, a simple adjustment on R at the near surface R_s is conducted in the current study.

The original data of R_s (i.e., $R_{s,\mathrm{org}}$) are simply compensated for with AF and converted to the adjusted data of R_s (i.e., $R_{s,\mathrm{adj}}$) as follows:

$$R_{s,\mathrm{adj}}(\mathrm{mm\ h^{-1}}) = R_{s,\mathrm{org}} \times 10^{-0.1\mathrm{AF}/b}(\mathrm{mm\ h^{-1}}). \tag{10}$$

In this study, b is 1.461 for the stratiform type and 1.544 for the convective and other types (Iguchi et al. 2009). The b

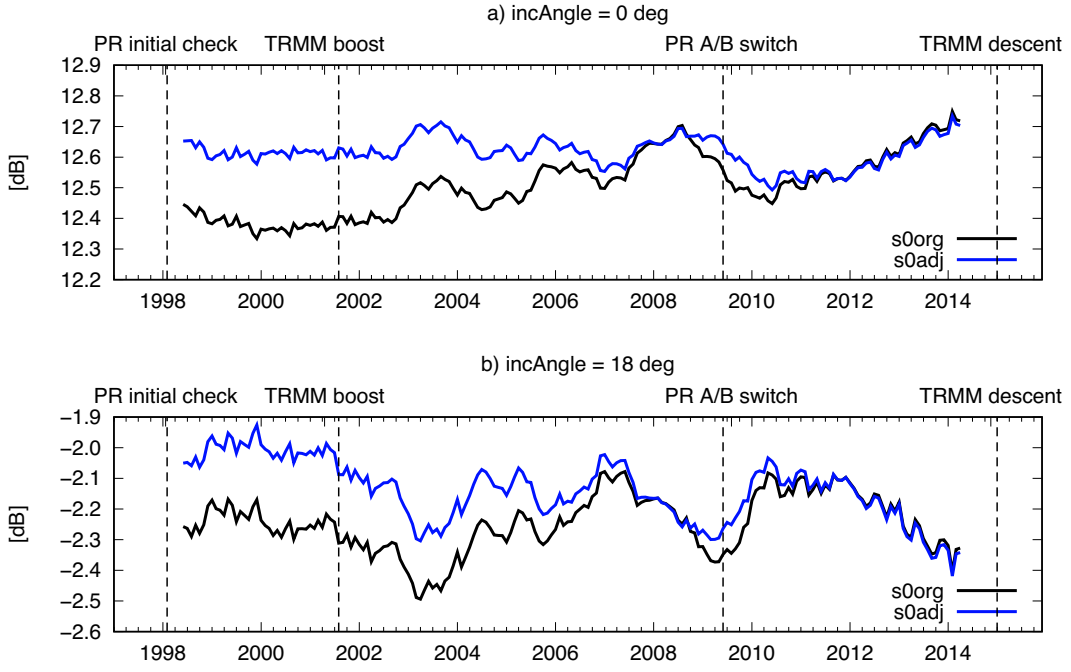

FIG. 6. Time series of σ^0_m obtained using the original (black line) and adjusted (blue line) data. Results are smoothed using a 13-month running average. (a) The nadir incidence (θ_z is about 0.1°). (b) The scan edge [θ_z is about 18.0° (18.1°) at the 350-km (403 km) operational period].

depends on precipitation types and its phase. Moreover, b is changed from an initial assumption of droplet size distribution (DSD) using a path-integrated attenuation (PIA) obtained from the surface echoes. As seen in Fig. 1, a relative change of R is changed with b so that possible uncertainty is contained in the current simple adjustment.

Figure 7 shows the precipitation time series of the PR data without and with the adjustment within the latitudinal band between 35°S and 35°N. The PR data at near-nadir angles (angle bins from 21 to 29) are only analyzed to mitigate a change in quality due to the TRMM orbit boost (Hirose et al. 2012). Moreover, the impact of the sensitivity degradation and

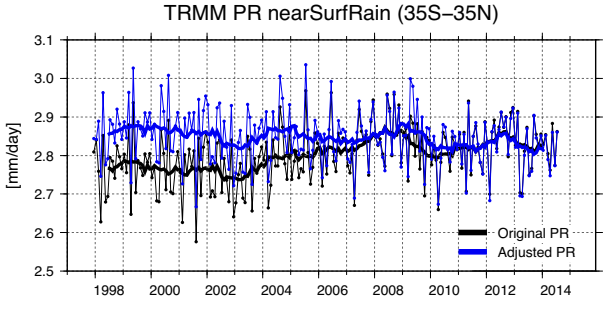

FIG. 7. Time series of the unconditional average for near-surface precipitation R_s (mm day^{-1}) within the latitudinal band between 35°S and 35°N. Black and blue lines indicate the original and adjusted PR data. Thick lines indicate the 13-month running averages. The data are used with near-nadir angles (angle bins from 21 to 29).

footprint size change due to the TRMM orbit boost on the unconditional average of precipitation at the surface was evaluated in the range from −0.5% to −2.1% (Shimizu et al. 2009; Kida et al. 2013; Kanemaru et al. 2015), and in this study, we use the change by −1.0% (Kanemaru et al. 2015). The impact due to the change in PR electronics was determined to be a −0.90% change (Kanemaru et al. 2017). Those impacts are simply applied to both original and adjusted data. The precipitation amount of the original PR data (black line in Fig. 7) gradually increases with time, whereas that of the adjusted PR data (blue line in Fig. 7) does not show such a gradual increase. Table 1 indicates the linear trends of the precipitation estimates obtained from the PR, TMI, and GPCP datasets over ocean, land, and both ocean and land surfaces. The TMI data are used only within the PR near-nadir (about 45 km wide) swath to remove the difference in swath width between the PR and TMI observations. For the PR dataset, the results with and without the calibration adjustment are also presented to evaluate the impact of the calibration adjustment on the trend analysis. As seen in Fig. 7, a positive trend obtained from the original PR data is found over the ocean plus land surfaces, but the trend obtained from the adjusted PR data has a small negative value over the ocean plus land surfaces. Therefore, the original PR data are overestimated by 0.082 mm (=0.059 + 0.023) day^{-1} decade^{-1} or 2.89% (=2.10 + 0.79) decade^{-1} due to the small temporal change in the PR calibration.

The original PR result of the linear trend without the adjustment is overall higher than the other results of the TMI and GPCP datasets (Fig. 8a), whereas the adjusted PR result

TABLE 1. Linear trends estimated from precipitation products. The unit is mm day^{-1} decade^{-1} (% decade^{-1} in parentheses). Products are analyzed from January 1998 to December 2013 within the latitudinal band between 35°S and 35°N. The symbol ± indicates the error of the linear slope.

35°S–35°N	Original PR	Adjusted PR	TMI	GPCP
Ocean + land	0.059 ± 0.011	−0.023 ± 0.011	0.029 ± 0.016	−0.007 ± 0.014
	(2.10 ± 0.39)	(−0.79 ± 0.39)	(1.06 ± 0.59)	(−0.23 ± 0.45)
Ocean	0.055 ± 0.018	−0.020 ± 0.019	0.026 ± 0.028	−0.023 ± 0.028
	(2.11 ± 0.71)	(−0.76 ± 0.72)	(0.97 ± 1.03)	(−0.78 ± 0.95)
Land	0.064 ± 0.027	−0.026 ± 0.027	0.034 ± 0.028	0.015 ± 0.030
	(2.08 ± 0.88)	(−0.83 ± 0.86)	(1.19 ± 0.97)	(0.45 ± 0.90)

tends to be underestimated compared with the other results. However, there is also a difference in the trend between the TMI and GPCP products. The trend of the TMI data in TRMM, version 7, is 0.029 ± 0.016 mm day^{-1} decade^{-1}, whereas that of the GPCP data is −0.007 ± 0.014 mm day^{-1} decade^{-1}. The GPCP products do not contain the TMI data so that the magnitude of the trend depends on the difference in data quality between the used data.

The disagreement of linear trends among the datasets during the TRMM period from January 1998 to December 2013 (Fig. 8a and Table 1) is mitigated when the analysis period is changed to the 403-km operation of the TRMM satellite from January 2002 to December 2013 (Fig. 8b and Table 2). Those results suggest that the discontinuity of data quality due to the TRMM orbit boost remains in the PR and TMI data (DeMoss and Bowman 2007; Shimizu et al. 2009).

Although the disagreement of linear trends is found among the datasets over the TRMM period, the pattern of global maps of the linear trend over the TRMM coverage is similar (Fig. 9). These trends are associated with various climate oscillations analyzed during the TRMM period (Wentz 2015), although changes in the interannual variability of precipitation are different among datasets (e.g., Wang et al. 2008; Henderson et al. 2017).

5. Summary

In this study, we investigate the temporal change in the PR calibration in TRMM, version 7, products to develop a precipitation climate record from the spaceborne precipitation radar data of the TRMM and following satellite missions. Since the PR measures the σ^0 over the ocean surface, the temporal change in the apparent σ^0 at incidence angles in which its variation is insensitive to the sea surface wind is considered as the temporal change in the PR calibration. The surface cross section σ^0 measured by the PR and the sea surface wind estimated from the simultaneous measurement of brightness temperature by the TMI are analyzed to detect the temporal change in the PR calibration. A small temporal change in the PR calibration of 0.19 dB decade^{-1} from 1998 to 2013 is found in the version 7 products, and the calibration constant is simply adjusted to evaluate impacts on the σ^0 time series and the precipitation trend analysis.

The original σ^0 time series at nadir and off-nadir angles are weakly positively correlated, whereas the adjusted ones are negatively correlated. This result is consistent with the surface wind speed dependence of σ^0 at nadir and off-nadir angles and indicates that the PR calibration change affects the analysis of the interannual variability of the σ^0 related to the sea surface wind. A linear trend of near-surface precipitation amount obtained from the PR data over most of the TRMM period (from January 1998 to December 2013) is changed from 0.059 mm day^{-1} decade^{-1} or 2.10% decade^{-1} to −0.023 mm day^{-1} decade^{-1} or −0.79% decade^{-1} with the temporal adjustment of the calibration change. The result indicates a 0.08 mm day^{-1} decade^{-1} or 2.9% decade^{-1} overestimation of the trend in the near-surface precipitation amount in the PR version 7 products. The trend

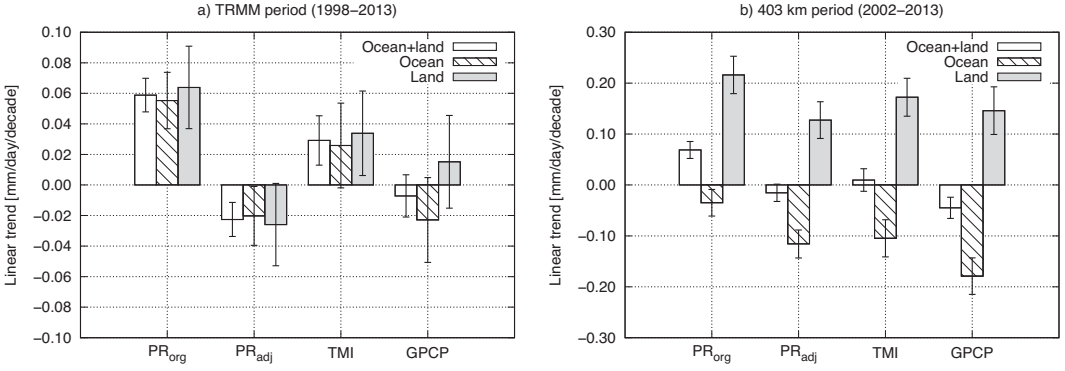

FIG. 8. Linear trends of R_s estimated from precipitation products. The unit is mm day^{-1} decade^{-1} within the latitudinal band between 35°S and 35°N. Error bars indicate the error of the linear slope. (a) TRMM period from January 1998 to December 2013 (192 months). (b) The 403-km operational period of TRMM satellite from January 2002 to December 2013 (144 months).

TABLE 2. As in Table 1, but for the period after the TRMM orbit boost from January 2002 to December 2013.

35°S–35°N	Original PR	Adjusted PR	TMI	GPCP
Ocean + land	0.069 ± 0.017	−0.015 ± 0.017	0.010 ± 0.022	−0.045 ± 0.021
	(2.45 ± 0.59)	(−0.54 ± 0.60)	(0.35 ± 0.81)	(−1.44 ± 0.67)
Ocean	−0.035 ± 0.026	−0.116 ± 0.027	−0.010 ± 0.0346	−0.179 ± 0.036
	(−1.32 ± 0.99)	(−4.35 ± 1.03)	(−3.88 ± 1.35)	(−6.88 ± 1.22)
Land	0.216 ± 0.037	0.127 ± 0.036	0.172 ± 0.037	0.146 ± 0.047
	(7.07 ± 1.20)	(4.12 ± 1.17)	(6.07 ± 1.31)	(4.35 ± 1.40)

analysis for datasets of PR, TMI, and GPCP is conducted to evaluate the consistency among datasets. The results differ among the PR data after the adjustment, the TMI data, and the GPCP data when the analyzed period is during the entire TRMM period. However, the disagreement is mitigated when the analyzed period is changed to the 403-km operational period after the TRMM orbit boost. Since the PR and TMI data have experienced the TRMM orbit boost, further evaluation of the data quality is required to use the plausible trend analysis.

The PR level-2 products in TRMM, versions 8 and 9, released in 2018 and 2022, respectively, have been reprocessed and provided by Japan Aerospace Exploration Agency (JAXA) and National Aeronautics and Space Administration (NASA). The PR level-2 products in TRMM, versions 8 and 9, have taken into account the temporal adjustment of the calibration change based upon the results of this study; σ_m^0 and Z_m are, respectively, adjusted as shown in (8) and (9). The PR calibration in TRMM, versions 8 and 9, is different from that in TRMM, version 7 (Masaki et al. 2022), so that the actual values of AF in versions 8 and 9 differ slightly from the values shown in this paper.

The current study focused on the calibration change in the TRMM PR, but the method developed in this study can be applied to the data of other spaceborne precipitation radars. The precipitation observations of the DPR on board the GPM *Core Observatory* began in March 2014, and its mission will be extended until the early 2030s (https://www.eorc.jaxa.jp/GPM/en/boost.html). In June 2023, the Precipitation Measuring Mission (PMM) was approved and the development of the Ku-band Doppler Precipitation Radar (KuDPR) started in Japan. The PMM satellite is scheduled to be launched in 2029. The Ku-band spaceborne precipitation radars of PR/KuPR/KuDPR will provide precipitation data record longer than 30 years from 1998 to 2030s. The current study would be helpful to investigate the calibration stability of the radars and the intercalibration among the radars.

Acknowledgments. The authors thank Kinji Furukawa of the Japan Aerospace Exploration Agency (JAXA), Tomohiko Higashiuwatoko of the Remote Sensing Technology Center of Japan (RESTEC), and Hiroshi Hanado and Katsuhiro Nakagawa of the National Institute of Information and Communications Technology (NICT) for providing valuable information and comments. The authors thank anonymous reviewers for valuable comments. This work was supported by JSPS KAKENHI Grant 22K04543.

Data availability statement. The TRMM PR and TMI, version 7, products are provided by JAXA (JAXA 1997b,a) and NASA (TRMM 2011) The TMI data are provided by Remote Sensing Systems (Wentz et al. 2015) and Colorado State University (Kummerow et al. 2011). The GPCP data are provided by NASA (Huffman et al. 2020).

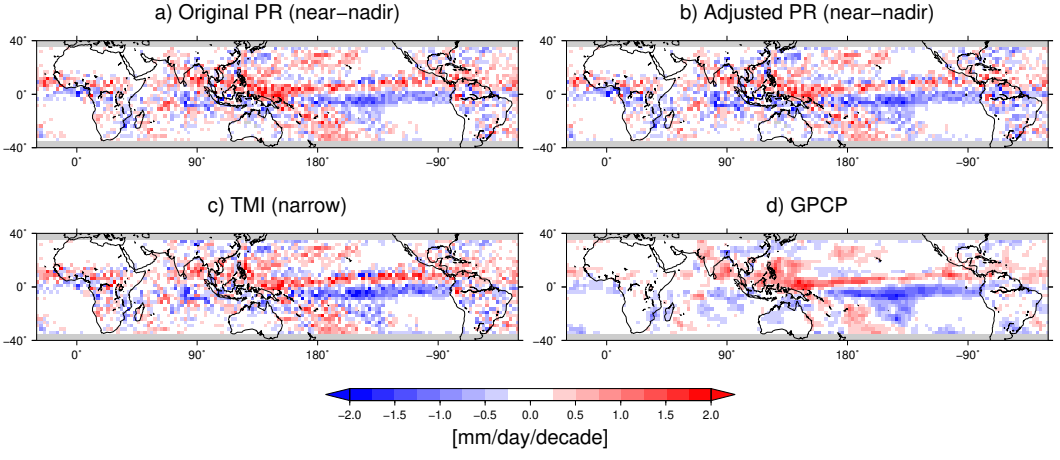

FIG. 9. Trend maps of the datasets over the TRMM period from January 1998 to December 2013. (a) Original PR. (b) Adjusted PR. (c) TMI. (d) GPCP. The PR data are analyzed at near-nadir angles. The TMI data are analyzed at the narrow swath matching the PR near-nadir swath.

REFERENCES

Adler, R. F., and Coauthors, 2018: The Global Precipitation Climatology Project (GPCP) monthly analysis (new version 2.3) and a review of 2017 global precipitation. *Atmosphere*, **9**, 138, https://doi.org/10.3390/atmos9040138.

Anagnostou, E. N., C. A. Morales, and T. Dinku, 2001: The use of TRMM precipitation radar observations in determining ground radar calibration biases. *J. Atmos. Oceanic Technol.*, **18**, 616–628, https://doi.org/10.1175/1520-0426(2001)018<0616:TUOTPR>2.0.CO;2.

Ashouri, H., K.-L. Hsu, S. Sorooshian, D. K. Braithwaite, K. R. Knapp, L. D. Cecil, B. R. Nelson, and O. P. Prat, 2015: PERSIANN-CDR: Daily precipitation climate data record from multisatellite observations for hydrological and climate studies. *Bull. Amer. Meteor. Soc.*, **96**, 69–83, https://doi.org/10.1175/BAMS-D-13-00068.1.

Awaka, J., T. Iguchi, and K. Okamoto, 2009: TRMM PR standard algorithm 2A23 and its performance on bright band detection. *J. Meteor. Soc. Japan*, **87A**, 31–52, https://doi.org/10.2151/jmsj.87A.31.

Barrick, D., 1974: Wind dependence of quasi-specular microwave sea scatter. *IEEE Trans. Antennas Propag.*, **22**, 135–136, https://doi.org/10.1109/TAP.1974.1140736.

Berg, W., 2017: Towards developing a long-term high-quality intercalibrated TRMM/GPM radiometer dataset. *2017 IEEE Int. Geoscience and Remote Sensing Symp. (IGARSS)*, Fort Worth, TX, Institute of Electrical and Electronics Engineers, 248–250, https://doi.org/10.1109/IGARSS.2017.8126941.

——, and Coauthors, 2016: Intercalibration of the GPM microwave radiometer constellation. *J. Atmos. Oceanic Technol.*, **33**, 2639–2654, https://doi.org/10.1175/JTECH-D-16-0100.1.

Colton, M. C., and G. A. Poe, 1999: Intersensor calibration of DMSP SSM/I's: F-8 to F-14, 1987-1997. *IEEE Trans. Geosci. Remote Sens.*, **37**, 418–439, https://doi.org/10.1109/36.739079.

Crisologo, I., R. A. Warren, K. Mühlbauer, and M. Heistermann, 2018: Enhancing the consistency of spaceborne and ground-based radar comparisons by using beam blockage fraction as a quality filter. *Atmos. Meas. Tech.*, **11**, 5223–5236, https://doi.org/10.5194/amt-11-5223-2018.

DeMoss, J. D., and K. P. Bowman, 2007: Changes in TRMM rainfall due to the orbit boost estimated from buoy rain gauge data. *J. Atmos. Oceanic Technol.*, **24**, 1598–1607, https://doi.org/10.1175/JTECH2082.1.

Freilich, M. H., and B. A. Vanhoff, 2003: The relationship between winds, surface roughness, and radar backscatter at low incidence angles from TRMM precipitation radar measurements. *J. Atmos. Oceanic Technol.*, **20**, 549–562, https://doi.org/10.1175/1520-0426(2003)20%3C549:TRBWSR%3E2.0.CO;2.

Han, J., Z. Chu, Z. Wang, D. Xu, N. Li, L. Kou, F. Xu, and Y. Zhu, 2018: The establishment of optimal ground-based radar datasets by comparison and correlation analyses with spaceborne radar data. *Meteor. Appl.*, **25**, 161–170, https://doi.org/10.1002/met.1682.

Henderson, D. S., C. D. Kummerow, D. A. Marks, and W. Berg, 2017: A regime-based evaluation of TRMM oceanic precipitation biases. *J. Atmos. Oceanic Technol.*, **34**, 2613–2635, https://doi.org/10.1175/JTECH-D-16-0244.1.

——, ——, and W. Berg, 2018: ENSO influence on TRMM tropical oceanic precipitation characteristics and rain rates. *J. Climate*, **31**, 3979–3998, https://doi.org/10.1175/JCLI-D-17-0276.1.

Hirose, M., S. Shimizu, R. Oki, T. Iguchi, D. A. Short, and K. Nakamura, 2012: Incidence-angle dependency of TRMM PR rain estimates. *J. Atmos. Oceanic Technol.*, **29**, 192–206, https://doi.org/10.1175/JTECH-D-11-00067.1.

Hou, A. Y., and Coauthors, 2014: The Global Precipitation Measurement mission. *Bull. Amer. Meteor. Soc.*, **95**, 701–722, https://doi.org/10.1175/BAMS-D-13-00164.1.

Huffman, G. J., R. F. Adler, A. Behrangi, D. T. Bolvin, E. Nelkin, and Y. Song, 2020: Algorithm Theoretical Basis Document (ATBD) for Global Precipitation Climatology Project version 3.1 precipitation data, https://docserver.gesdisc.eosdis.nasa.gov/public/project/MEaSUREs/GPCP/GPCP_ATBD_V3.1.pdf.

——, ——, ——, ——, E. J. Nelkin, G. Gu, and M. R. Ehsani, 2023: The new version 3.2 Global Precipitation Climatology Project (GPCP) monthly and daily precipitation products. *J. Climate*, **36**, 7635–7655, https://doi.org/10.1175/JCLI-D-23-0123.1.

Iguchi, T., 2020: Dual-Frequency Precipitation Radar (DPR) on the Global Precipitation Measurement (GPM) mission's core observatory. *Satellite Precipitation Measurement*, V. Levizzani et al., Eds., Advances in Global Change Research, Vol. 67, Springer, 183–192, https://doi.org/10.1007/978-3-030-24568-9_11.

——, T. Kozu, R. Meneghini, J. Awaka, and K. Okamoto, 2000: Rain-profiling algorithm for the TRMM precipitation radar. *J. Appl. Meteor.*, **39**, 2038–2052, https://doi.org/10.1175/1520-0450(2001)040<2038:RPAFTT>2.0.CO;2.

——, ——, J. Kwiatkowski, R. Meneghini, J. Awaka, and K. Okamoto, 2009: Uncertainties in the rain profiling algorithm for the TRMM Precipitation Radar. *J. Meteor. Soc. Japan*, **87A**, 1–30, https://doi.org/10.2151/jmsj.87A.1.

——, and Coauthors, 2023: GPM/DPR Level-2 algorithm theoretical basis document. 265 pp., https://www.eorc.jaxa.jp/GPM/doc/algorithm/ATBD_DPR_L2.pdf.

IPCC, 2021: Changing state of the climate system. *Climate Change 2021: The Physical Science Basis*, V. Masson-Delmotte et al., Eds., Cambridge University Press, 287–422 pp., https://doi.org/10.1017/9781009157896.004.

JAXA, 1997a: TRMM/PR L2 rainfall profile. Accessed 11 July 2024, https://doi.org/10.57746/EO.01gs73b07qz30927ydax3m99fg.

——, 1997b: TRMM/PR L2 surface cross section. Accessed 11 July 2024, https://doi.org/10.57746/EO.01gs73b05w4k4mgk452amabay7.

Ji, L., W. Xu, H. Chen, and N. Liu, 2022: Consistency of vertical reflectivity profiles and echo-top heights between spaceborne radars onboard TRMM and GPM. *Remote Sens.*, **14**, 1987, https://doi.org/10.3390/rs14091987.

Kanemaru, K., T. Kubota, T. Iguchi, Y. N. Takayabu, and R. Oki, 2017: Development of a precipitation climate record from spaceborne precipitation radar data. Part I: Mitigation of the effects of switching to redundancy electronics in the TRMM precipitation radar. *J. Atmos. Oceanic Technol.*, **34**, 2043–2057, https://doi.org/10.1175/JTECH-D-17-0026.1.

——, ——, and ——, 2019: Improvements in the beam-mismatch correction of precipitation radar data after the TRMM orbit boost. *IEEE Trans. Geosci. Remote Sens.*, **57**, 7161–7169, https://doi.org/10.1109/TGRS.2019.2911990.

——, T. Iguchi, T. Masaki, and T. Kubota, 2020: Estimates of spaceborne precipitation radar pulsewidth and beamwidth using sea surface echo data. *IEEE Trans. Geosci. Remote Sens.*, **58**, 5291–5303, https://doi.org/10.1109/TGRS.2019.2963090.

Kanemaru, S., K. Kida, T. Kubota, M. Kachi, R. Oki, T. Iguchi, and Y. Takayabu, 2015: Creation of TRMM PR data by minimizing the effect of the TRMM orbit boost. *30th Int. Symp. on Space Technology and Science*, Kobe, Japan, The Japan Society for Aeronautical and Space Sciences, 1–6, https://archive.ists.ne.jp/upload_pdf/2015-n-12.pdf.

Kida, S., T. Kubota, M. Kachi, R. Oki, T. Iguchi, and Y. N. Takayabu, 2013: Reduction of discontinuity due to the orbit boost in TRMM Precipitation Radar product for climate studies. *2013 IEEE Int. Geoscience and Remote Sensing Symp. (IGARSS)*, Melbourne, Victoria, Australia, Institute of Electrical and Electronics Engineers, 644–647, https://doi.org/10.1109/IGARSS.2013.6721239.

Kim, J.-H., M.-L. Ou, J.-D. Park, K. R. Morris, M. R. Schwaller, and D. B. Wolff, 2014: Global Precipitation Measurement (GPM) ground validation (GV) prototype in the Korean Peninsula. *J. Atmos. Oceanic Technol.*, **31**, 1902–1921, https://doi.org/10.1175/JTECH-D-13-00193.1.

Klein, L., and C. Swift, 1977: An improved model for the dielectric constant of sea water at microwave frequencies. *IEEE J. Oceanic Eng.*, **2**, 104–111, https://doi.org/10.1109/JOE.1977.1145319.

Kojima, M., and Coauthors, 2012: Dual-frequency Precipitation Radar (DPR) development on the Global Precipitation Measurement (GPM) core observatory. *Proc. SPIE*, **8528**, 85281A, https://doi.org/10.1117/12.976823.

Komukai, J., K. Okamoto, S. Shige, and T. Manabe, 2010: Analysis of surface normalized radar cross section for the improvement of the TRMM Precipitation Radar algorithm. PART I: Over the ocean (in Japanese). *J. Remote Sens. Soc. Japan*, **30**, 221–233, https://doi.org/10.11440/rssj.30.221.

Kozu, T., 1995: A generalized surface echo radar equation for down-looking pencil beam radar. *IEICE Trans. Commun.*, **78**, 1245–1248.

——, and Coauthors, 2001: Development of precipitation radar onboard the Tropical Rainfall Measuring Mission (TRMM) satellite. *IEEE Trans. Geosci. Remote Sens.*, **39**, 102–116, https://doi.org/10.1109/36.898669.

——, T. Iguchi, T. Shimomai, and N. Kashiwagi, 2009: Raindrop size distribution modeling from a statistical rain parameter relation and its application to the TRMM precipitation radar rain retrieval algorithm. *J. Appl. Meteor. Climatol.*, **48**, 716–724, https://doi.org/10.1175/2008JAMC1998.1.

Kumagai, H., K. Toshiaki, and T. Iguchi, 1996: Development of an algorithm for rain/no-rain discrimination (in Japanese). *Rev. Commun. Res. Lab*, **42**, 317–323.

Kummerow, C., W. Barnes, T. Kozu, J. Shiue, and J. Simpson, 1998: The Tropical Rainfall Measuring Mission (TRMM) sensor package. *J. Atmos. Oceanic Technol.*, **15**, 809–817, https://doi.org/10.1175/1520-0426(1998)015<0809:TTRMMT>2.0.CO;2.

——, and Coauthors, 2001: The evolution of the Goddard profiling algorithm (GPROF) for rainfall estimation from passive microwave sensors. *J. Appl. Meteor.*, **40**, 1801–1820, https://doi.org/10.1175/1520-0450(2001)040<1801:TEOTGP>2.0.CO;2.

Kummerow, C. D., S. Ringerud, J. Crook, D. Randel, and W. Berg, 2011: An observationally generated a priori database for microwave rainfall retrievals. *J. Atmos. Oceanic Technol.*, **28**, 113–130, https://doi.org/10.1175/2010JTECHA1468.1.

Li, L., E. Im, S. L. Durden, and Z. S. Haddad, 2002: A surface wind model–based method to estimate rain-induced radar path attenuation over ocean. *J. Atmos. Oceanic Technol.*, **19**, 658–672, https://doi.org/10.1175/1520-0426(2002)019<0658:ASWMBM>2.0.CO;2.

Masaki, T., T. Iguchi, K. Kanemaru, K. Furukawa, N. Yoshida, T. Kubota, and R. Oki, 2022: Calibration of the dual-frequency precipitation radar onboard the Global Precipitation Measurement Core Observatory. *IEEE Trans. Geosci. Remote Sens.*, **60**, 1–16, https://doi.org/10.1109/TGRS.2020.3039978.

Meneghini, R., T. Iguchi, T. Kozu, L. Liao, K. Okamoto, J. A. Jones, and J. Kwiatkowski, 2000: Use of the surface reference technique for path attenuation estimates from the TRMM precipitation radar. *J. Appl. Meteor.*, **39**, 2053–2070, https://doi.org/10.1175/1520-0450(2001)040<2053:UOTSRT>2.0.CO;2.

Munchak, S. J., R. Meneghini, M. Grecu, and W. S. Olson, 2016: A consistent treatment of microwave emissivity and radar backscatter for retrieval of precipitation over water surfaces. *J. Atmos. Oceanic Technol.*, **33**, 215–229, https://doi.org/10.1175/JTECH-D-15-0069.1.

Nakamura, K., 2021: Progress from TRMM to GPM. *J. Meteor. Soc. Japan*, **99**, 697–729, https://doi.org/10.2151/jmsj.2021-035.

Sapiano, M. R. P., W. K. Berg, D. S. McKague, and C. D. Kummerow, 2013: Toward an intercalibrated fundamental climate data record of the SSM/I sensors. *IEEE Trans. Geosci. Remote Sens.*, **51**, 1492–1503, https://doi.org/10.1109/TGRS.2012.2206601.

Schumacher, C., and R. A. Houze Jr., 2003: Stratiform rain in the tropics as seen by the TRMM Precipitation Radar. *J. Climate*, **16**, 1739–1756, https://doi.org/10.1175/1520-0442(2003)016%3C1739:SRITTA%3E2.0.CO;2.

Shimizu, S., R. Oki, T. Tagawa, T. Iguchi, and M. Hirose, 2009: Evaluation of the effects of the orbit boost of the TRMM satellite on PR rain estimates. *J. Meteor. Soc. Japan*, **87A**, 83–92, https://doi.org/10.2151/jmsj.87A.83.

Silberstein, D. S., D. B. Wolff, D. A. Marks, D. Atlas, and J. L. Pippitt, 2008: Ground clutter as a monitor of radar stability at Kwajalein, RMI. *J. Atmos. Oceanic Technol.*, **25**, 2037–2045, https://doi.org/10.1175/2008JTECHA1063.1.

Skofronick-Jackson, G., and Coauthors, 2017: The Global Precipitation Measurement (GPM) mission for science and society. *Bull. Amer. Meteor. Soc.*, **98**, 1679–1695, https://doi.org/10.1175/BAMS-D-15-00306.1.

Stocker, E. F., F. Alquaied, S. Bilanow, Y. Ji, and L. Jones, 2018: TRMM version 8 reprocessing improvements and incorporation into the GPM data suite. *J. Atmos. Oceanic Technol.*, **35**, 1181–1199, https://doi.org/10.1175/JTECH-D-17-0166.1.

Tagawa, T., H. Hanado, S. Shimizu, and R. Oki, 2009: Improved correction of beam mismatch of the precipitation radar after orbit boost of the TRMM satellite. *IEEE Trans. Geosci. Remote Sens.*, **47**, 3469–3479, https://doi.org/10.1109/TGRS.2009.2020914.

Takahashi, H. G., and H. Fujinami, 2021: Recent decadal enhancement of Meiyu–Baiu heavy rainfall over East Asia. *Sci. Rep.*, **11**, 13665, https://doi.org/10.1038/s41598-021-93006-0.

Takahashi, N., and T. Iguchi, 2004: Estimation and correction of beam mismatch of the Precipitation Radar after an orbit boost of the tropical rainfall measuring mission Satellite. *IEEE Trans. Geosci. Remote Sens.*, **42**, 2362–2369, https://doi.org/10.1109/TGRS.2004.837334.

——, and ——, 2008: Characteristics of TRMM/PR system noise and their application to the rain detection algorithm. *IEEE Trans. Geosci. Remote Sens.*, **46**, 1697–1704, https://doi.org/10.1109/TGRS.2008.916205.

——, H. Kuroiwa, and T. Kawanishi, 2003: Four-year result of external calibration for Precipitation Radar (PR) of the Tropical

Rainfall Measuring Mission (TRMM) satellite. *IEEE Trans. Geosci. Remote Sens.*, **41**, 2398–2403, https://doi.org/10.1109/TGRS.2003.817180.

——, and Coauthors, 2016: Overview of the end-of-mission observation experiments of Precipitation Radar onboard the tropical rainfall measuring mission satellite. *IEEE Trans. Geosci. Remote Sens.*, **54**, 3450–3459, https://doi.org/10.1109/TGRS.2016.2518221.

TRMM PR Team, 2011: Tropical Rainfall Measuring Mission (TRMM) precipitation radar algorithm instruction manual for version 7. 175 pp., https://www.eorc.jaxa.jp/TRMM/documents/PR_algorithm_product_information/pr_manual/PR_Instruction_Manual_V7_L1.pdf.

TRMM, 2011: TRMM microwave imager hydrometeor profile L2 1.5 hours V7. Goddard Earth Sciences Data and Information Services Center (GES DISC), https://data.nasa.gov/dataset/TRMM-Microwave-Imager-Hydrometeor-Profile-L2-1-5-h/ck99-fg5h/data?no_mobile=true.

Valenzuela, G. R., 1978: Theories for the interaction of electromagnetic and oceanic waves—A review. *Bound.-Layer Meteor.*, **13**, 61–85, https://doi.org/10.1007/BF00913863.

Wang, J.-J., R. F. Adler, and G. Gu, 2008: Tropical rainfall-surface temperature relations using Tropical Rainfall Measuring Mission precipitation data. *J. Geophys. Res.*, **113**, D18115, https://doi.org/10.1029/2007JD009540.

Warren, R. A., A. Protat, S. T. Siems, H. A. Ramsay, V. Louf, M. J. Manton, and T. A. Kane, 2018: Calibrating ground-based radars against TRMM and GPM. *J. Atmos. Oceanic Technol.*, **35**, 323–346, https://doi.org/10.1175/JTECH-D-17-0128.1.

Wentz, F. J., 2013: SSM/I version-7 calibration report. Remote Sensing Systems Tech. Rep. 11012, 46 pp., https://images.remss.com/papers/rsstech/2012_011012_Wentz_Version-7_SSMI_Calibration.Pdf.

——, 2015: A 17-yr climate record of environmental parameters derived from the Tropical Rainfall Measuring Mission (TRMM) microwave imager. *J. Climate*, **28**, 6882–6902, https://doi.org/10.1175/JCLI-D-15-0155.1.

——, S. Peteherych, and L. A. Thomas, 1984: A model function for ocean radar cross sections at 14.6 GHz. *J. Geophys. Res.*, **89**, 3689–3704, https://doi.org/10.1029/JC089iC03p03689.

——, P. Ashcroft, and C. Gentemann, 2001: Post-launch calibration of the TRMM microwave imager. *IEEE Trans. Geosci. Remote Sens.*, **39**, 415–422, https://doi.org/10.1109/36.905249.

——, C. Gentemann, and K. Hilburn, 2015: Remote sensing systems TRMM TMI daily environmental suite on 0.25 deg grid, Version 7.1. Remote Sensing Systems, www.remss.com/missions/tmi.

Xie, P., and P. A. Arkin, 1997: Global precipitation: A 17-year monthly analysis based on gauge observations, satellite estimates, and numerical model outputs. *Bull. Amer. Meteor. Soc.*, **78**, 2539–2558, https://doi.org/10.1175/1520-0477(1997)078<2539:GPAYMA>2.0.CO;2.

Yan, B., and F. Weng, 2008: Intercalibration between special sensor microwave imager/sounder and special sensor microwave imager. *IEEE Trans. Geosci. Remote Sens.*, **46**, 984–995, https://doi.org/10.1109/TGRS.2008.915752.

Zhang, S., Y. Zhu, Z. Wang, and Y. Wang, 2018: Consistency analysis and correction of ground-based radar observations using space-borne radar. *J. Atmos. Sol.-Terr. Phys.*, **169**, 114–121, https://doi.org/10.1016/j.jastp.2018.01.030.